

Effect of nano-sized precipitates on the fatigue property of a lamellar structured high entropy alloy

Kaimiao Liu^a, Bharat Gwalani^b, Mageshwari Komarasamy^a, Shivakant Shukla^a, Tianhao Wang^a, Rajiv S. Mishra^{a,b*}

^aCenter for Friction Stir Processing

Department of Materials Science and Engineering

^bAdvanced Materials and Manufacturing Processes Institute

University of North Texas, Denton, TX 76207 USA

*Corresponding author: email ID — Rajiv.Mishra@unt.edu

Abstract

Fatigue damage is inevitable and destructive for in-service structural materials and hence warrants a detailed examination of the fatigue behavior of potential structural materials such as high entropy alloys (HEAs). This study focused on investigation of the mechanical properties of Al_{0.7}CoCrFeNi HEA with two microstructural conditions; i.e., a lamellar structure consisting of FCC+B2 phases (a) without precipitates and (b) with nano-sized L1₂ precipitates in the FCC phase. Nano-sized L1₂ precipitates were introduced in FCC through low-temperature annealing. Although the nano-sized L1₂ precipitates enhanced tensile strength, no improvement in fatigue properties was noted. For both conditions, crack initiation and propagation were observed along persistent slip bands and FCC/B2 phase boundaries.

Keywords: fatigue; high entropy alloy; lamellar microstructure; persistent slip bands

1. Introduction

Independently, Yeh et al. [1] and Cantor et al. [2] first introduced a new class of alloys generally referred as high entropy alloys (HEAs), which consist of five or more principal elements in equiatomic or non-equiatomic compositions. These alloys have recently been termed complex concentrated alloys (CCAs), due to the inclusion of alloys with a minimum of three principal elements and alloys with intermetallic second phases [1,3-7]. The shift in compositional space

from edges or apexes of a phase diagram towards the center has increased flexibility in tuning the composition and enables subsequent microstructural engineering. In these compositionally complex alloys, strengthening mechanisms such as solid solution strengthening, precipitation strengthening, grain boundary strengthening, and transformation hardening could be used to attain an exceptional combination of properties [1,3,4,6,8,9]. One of the CCAs investigated in detail is $\text{Al}_x\text{CoCrFeNi}$, where second-phase precipitates form when Al content ≥ 0.3 mole fraction. With increasing Al content, the alloy transforms from single-phase face-centered cubic (FCC) structure to FCC+B2 (NiAl-rich), then to body-centered cubic (BCC/B2) + FCC, and finally to single-phase BCC, owing to the strong tendency for the formation of B2 with Al and Ni [5,7]. In the $\text{Al}_{x(\geq 0.3)}\text{CoCrFeNi}$ alloy system, typically strength and ductility are enhanced with the presence of high-strength B2 phase and ductile FCC matrix. During deformation of such a duplex alloy, low stacking fault energy (SFE) of the FCC phase promotes the formation of stacking faults and deformation twins [10]. These defects are known to provide obstacles to dislocation motion and to aid in dislocation storage that enhances workability. In $\text{Al}_x\text{CoCrFeNi}$, when Al content reaches 0.7 mole fraction, a lamellar microstructure composed of B2 and FCC phases with a semi-coherent interface is formed [7]. During monotonic testing, nano-precipitate strengthening of FCC matrix [11] and additional boundary strengthening with narrow interlamellar spacing in $\text{Al}_{0.7}\text{CoCrFeNi}$ [12] have occurred. Despite extensive investigations into microstructures and tensile properties, only six studies into fatigue property assessment of HEAs have been reported [13-18].

Fatigue causes cumulative damage to the materials due to cyclic loading that leads to destructive failure of in-service structural materials [19-21]. Since HEAs have shown immense promise in simultaneous enhancement of strength and ductility by microstructural tuning, these alloys are

potential candidates for structural applications [22]. Thus, examination of the fatigue response of these HEAs also becomes very important. The fatigue behavior of cold-rolled Al_{0.5}CoCrCuFeNi was investigated by Hemphill et al. [15], where fatigue failure initiated from Al₂O₃ inclusions and pre-existing microcracks. After rolling and annealing of the same alloy, Tang et al. [16] concluded that fatigue crack began at the shrinkage pores. Furthermore, the same alloy made with high-purity elements exhibited better fatigue as compared to the alloy with low-purity elements. Recently, excellent fatigue properties of an ultrafine-grained triplex Al_{0.3}CoCrFeNi HEA regardless of the presence of hard phases were attributed to the formation of deformation nanotwins during cyclic loading [13].

During fatigue deformation of coarse-grained materials, the formation of persistent slip bands (PSBs) is well-known to severely affect fatigue crack initiation, propagation, and subsequent failure [23]. PSBs generally result from the localization of cyclic plastic deformation in a few slip systems and the continuation of plastic deformation in those slip systems. PSBs have been proven as fatigue crack initiation and propagation mechanisms [21,24]. Cyclic plastic deformation within the PSBs generates surface extrusions and intrusions along active slip planes [25]. Subsequently, surface intrusions and extrusions become fatigue crack initiation sites [19,24]. In some cases, a zigzag crack growth path observed during cyclic loading was a consequence of the activation of multiple slip systems and subsequent PSB formation [26]. In HEAs, the effect of PSBs in influencing fatigue property has been reported only by Shukla et al. [14] where the fatigue behavior of as-cast and cold-rolled annealed AlCoCrFeNi_{2.1} was compared. In as-cast condition, the crack initiated in FCC lamellar along PSB boundaries. In cold-rolled + annealed condition, however, crack initiation was delayed due to the presence of B2 precipitates, which subsequently led to enhanced fatigue properties.

In addition to B2 precipitation in $\text{Al}_{0.3-0.7}\text{CoCrFeNi}$ HEAs, Ni_3Al -type (L1_2) precipitates are also formed during relatively low-temperature aging. These nano-sized L1_2 precipitates increase material strength during monotonic deformation [27]. Therefore, in the current endeavor, the effect of L1_2 precipitates on the fatigue properties of $\text{Al}_{0.7}\text{CoCrFeNi}$ CCA was investigated. For comparison, material homogenized at high temperature without subsequent aging heat treatment to form L1_2 precipitates was also examined. For both conditions, detailed initial microstructural characterization, monotonic and cyclic property analyses, and post-fatigue deformation characterization were carried out.

2. Methods

2.1 Material processing

The alloy prepared using vacuum arc melting was obtained from Sophisticated Alloys, Inc. The cast samples were hot-rolled to 30% thickness reduction at 1150°C , and then cold-rolled to achieve an additional 30% thickness reduction. Two different heat treatment routes were followed (Figure 1). In the first route, homogenization at 1100°C for 10 minutes followed by water quenching results in what is referred to as the homogenized (AH) condition. Elemental segregation and rolling strain were eliminated during high-temperature homogenization heat treatment. In the second route, the cold-rolled + homogenized material was subsequently annealed at 580°C for 24 hours to form L1_2 precipitates, which henceforth are denoted as as-homogenized + low-temperature annealing (AH+LTA) condition. Therefore, two distinct microstructures were obtained upon heat treatment. Pandat and PanHEA databases were used to predict phases that are attained through different heat treatment paths.

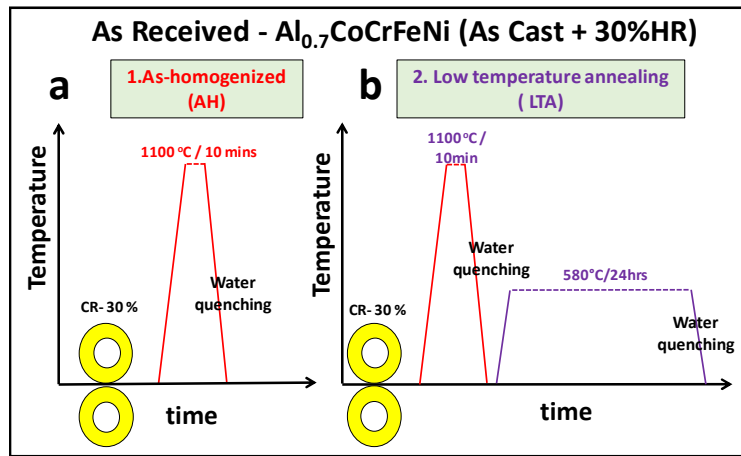


Figure 1. A schematic illustrating the two different processing routes to engineer the microstructure of $\text{Al}_{0.7}\text{CoCrFeNi}$.

2.2 Microstructural characterization

Back-scattered electron (BSE) microscopy and electron backscattered diffraction (EBSD) analysis were carried out on the FEI Nova NanoSEM230 fitted with Hikari super EBSD system. X-ray diffraction (XRD) with Rigaku Ultima III high-resolution XRD with $\text{Cu K}\alpha$ radiation was used for phase analysis. TEM analysis was conducted before and after fatigue testing using FEI Tecnai G2 TF20TM at 200 kV, and samples were prepared using a focused ion beam (FIB) (FEI Nova 200 NanoLab).

2.3 Mechanical testing

Sub-sized tensile and fatigue specimens were milled with a computer numerical control machine. Tensile samples with gage length \sim 5 mm, width \sim 1.2 mm, and thickness \sim 1.1 mm were tested using a computer-controlled mini-tensile machine at an initial strain rate of 10^{-3} s^{-1} . Total elongation was obtained from an LVDT (linear variable displacement transformer) extensometer. Three independent tensile tests confirmed tensile elongation and strength. Fully reversed ($R=-1$) bending fatigue tests were performed with a custom-made tabletop fatigue testing machine. Frequency of the cyclic loading was 20 Hz. Sample dimensions and machine details are given in

[28]. The fractured samples were preserved to conduct fractography. Tensile and fatigue samples were polished with SiC papers to 1200 grit, and final polishing with 1 μm diamond suspension. Fatigue samples subjected to microscopy were further polished with 0.05 and 0.02 μm colloidal silica suspensions.

3. Results and Discussion

3.1 Initial microstructures

Microstructural analysis of AH and AH+LTA conditions is presented in Figure 2. High-temperature heat treatment was carried out to homogenize the material while low-temperature heat treatment was done to form L₁₂ precipitates. The microstructure exhibited a near-eutectic lamellar structure composed of two phases in the AH condition. For both conditions, BSE images (Figures 2 (a, c)) revealed dark and light contrast phases. High-magnification BSE images of both conditions are displayed as insets in Figures 2 (a, c). EBSD phase analysis confirmed that the lamellar structure is comprised of BCC/B2 (B2 is an ordered bcc structure, green color coded in the figure) and FCC phase (red color-coded). Based on EBSD phase fraction analysis, AH condition had FCC and B2 fractions of 65% and 35%, respectively (Figure 2 (b)); and AH+LTA condition exhibited FCC and B2 fractions of 60% and 40%, respectively (Figure 2 (d)). The slight difference in phase fraction can be attributed solely to the spatial variation of phases. The lamellar width for AH condition is $1.2 \pm 0.8 \mu\text{m}$, and for AH+LTA condition is $1.1 \pm 0.2 \mu\text{m}$. XRD analysis (insets in Figures 2 (b), d)) shows distinct peaks for FCC and B2 phases for both conditions. According to the pseudo-binary phase diagram (Figure 2 (e)), low-temperature annealing heat treatment of 580°C is expected to facilitate the formation of nano-sized L₁₂ precipitates. Thus, detailed TEM analysis indeed confirmed the presence of L₁₂ precipitates in AH+LTA condition.

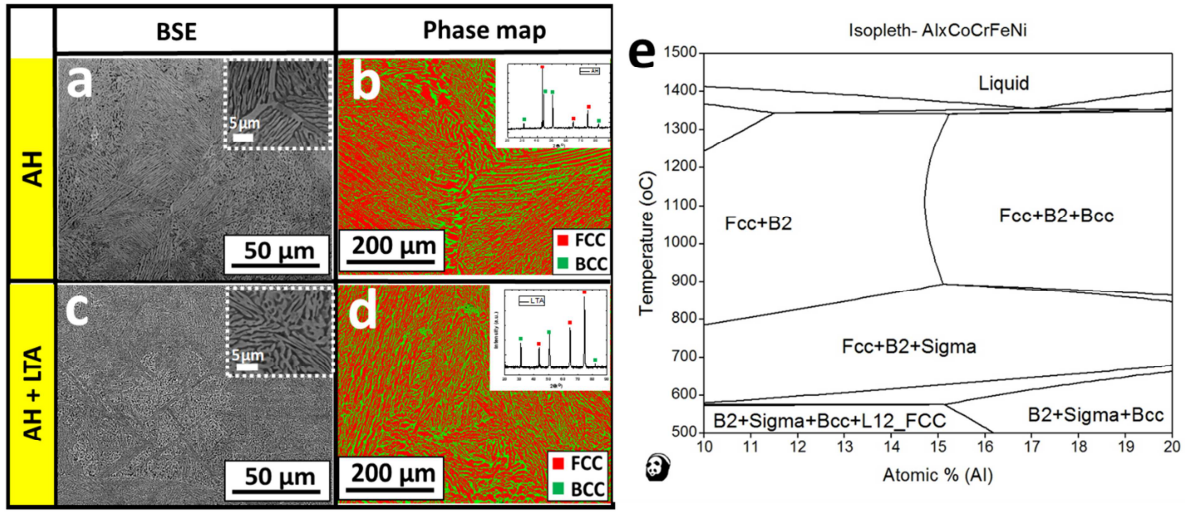


Figure 2. *Initial microstructural analysis for both conditions.* BSE image of the (a) as-homogenized (AH) and (c) low-temperature annealing (AH+LTA) conditions. High magnification BSE images in the insets confirmed lamellar structure. EBSD phase map of (b) AH and (d) AH+LTA conditions, with inset showing XRD analysis for both conditions, and (e) pseudo-binary phase diagram for $\text{Al}_x\text{CoCrFeNi}$ via Pandat.

The composition and crystallographic information of the various phases in the two heat treatment conditions are presented in Figure (3). Figure 3 (a), the bright field TEM (BFTEM) image taken from the AH condition, clearly shows the two lamellar phases. The micro-diffraction patterns from each of the lamellar phases (Figures 3 (a₁, a₂)) confirm that the pattern in Figure 3 (a₁) obtained from the bright contrast phase (in Figure 3 (a)) can be conclusively indexed to be [011]_{FCC}; whereas the pattern in Figure 3 (a₂) from the dark contrast phase indexed as [011]_{BCC}. The (001) superlattice spots in Figure 3 (a₂) prove ordering of the BCC phase. Selected area diffraction patterns (SADPs) from the FCC phase in AH+LTA condition in Figure 3 (c) include the SADPs from [112]_{FCC} and [111]_{FCC} (Figures 3 (c₁,c₂)). Note that the extra superlattice spots at (110) positions in AH+LTA condition (which were not seen in AH) confirm the ordering of the FCC phase in this condition. Compositional analysis by STEM-EDS in both conditions (Figures 3 (b, b₁₋₅, d, and d₁₋₅)) shows that the FCC phase is rich in Fe, Co, Cr; whereas the B2 (grey

contrast in Figure 3 (a)) is Al, Ni-rich and Fe, Co, Cr-lean. However, EDS maps highlight an extra L₁₂ phase in the AH+LTA condition, which is rich in Al and Ni, (Figure 3 (d, d₁₋₅). The average size of L₁₂ is 2.2 ± 1.3 nm. Hence, this hierarchical lamellar microstructure consisting of a eutectic B2 + FCC structure with nano-sized L₁₂ embedded within FCC is important for a detailed understanding of the effects of these microstructural features on the alloy's tensile and fatigue properties.

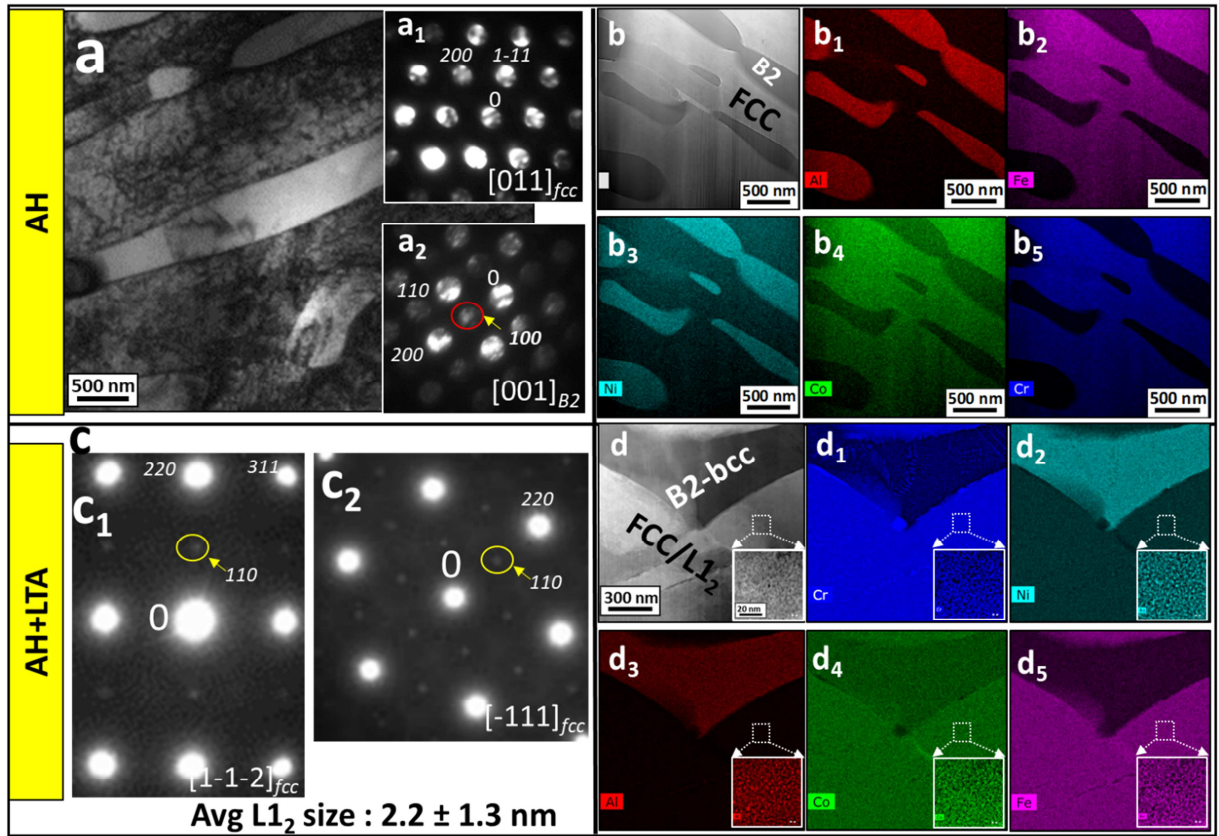


Figure 3. *Transmission electron microscopy results from both conditions.* (a) Bright field TEM image of AH condition, with FCC as dark contrast matrix phase and B2 as bright contrast phase; (a₁-a₂) shows the microdiffraction pattern of [011]_{FCC} zone axis and [001]_{B2} zone axis, respectively. (b) The HAADF-STEM image of AH condition, with FCC as white matrix phase and B2 as dark phase; (b₁-b₅) display the EDS-elemental distribution maps showing various elements as labeled in the figure. (c, c₁₋₂) are the SADPs of FCC phase from [112] and [111] zone axis respectively; superlattice reflections confirm the presence of L₁₂ phase. (d) The

HAADF-STEM image of AH condition, with FCC as bright contrast matrix phase and B2 as dark contrast phase; an additional dark contrast phase within FCC ($L1_2$ phase) is shown in the inset. (d₁-d₅) show EDS maps of various elements in the AH+LTA condition.

3.2 Mechanical properties

Engineering stress-strain curves for both conditions are presented in Figure 4 (a). As-homogenized (AH) $Al_{0.7}CoCrFeNi$ HEA showed yield strength (YS) of ~780 MPa, ultimate tensile strength (UTS) of ~1040 MPa, with plastic strain of ~17%. High strength in AH state is due to hard B2 phase and fine interlamellar spacing. Low-temperature annealed $Al_{0.7}CoCrFeNi$ exhibited YS of ~1050 MPa, UTS of ~1400 MPa and plastic strain of ~12%. The increase in strength in AH+LTA condition as compared with AH can be attributed to the coherent nano-sized $L1_2$ precipitates within the FCC phase (precipitation strengthening). However, the material's ability to store dislocations is reduced due to nano-sized shearable precipitates (strength-ductility trade-off) [6], hence a drop in ductility is observed in AH+LTA condition as compared with AH condition.

Stress amplitude [$\sigma_a = (\sigma_{max} - \sigma_{min})/2$] vs. fatigue life, (N_f), generally known as S-N curve, is plotted for both AH and AH+LTA conditions (Figure 4 (b)). No discernible difference in fatigue lives between AH and AH+LTA conditions was observed. Further, at higher stress amplitude region, AH condition exhibited better response. Fatigue endurance limits, which are defined as the maximum stress amplitudes to which the material is subjected for 10^7 cycles without failure, were ~460 MPa and ~410 MPa for AH+LTA and AH conditions, respectively. Scatter in data was observed in the S-N curves for both conditions. Therefore, we consider the differences observed in fatigue runout strength and high stress amplitude regime not to be significant as compared to the differences we observed under uniaxial tension testing. The fatigue ratios (R); i.e., the ratio of fatigue endurance limit to UTS for AH+LTA and AH

conditions, were ~ 0.33 and ~ 0.48 , respectively. Nano-sized L₁₂ precipitates increased material strength significantly. However, fatigue lives of the AH+LTA condition with L₁₂ precipitates were not improved as compared with AH condition. Various investigations on Ni-base superalloys have concluded that the size of L₁₂ precipitates has significant influence on fatigue and fracture properties [29,30]. The mechanism of dislocation-particle interaction changes with precipitate size. In under-aged condition, precipitate shearing occurs; while for over-aged condition, dislocation looping around the precipitates is the dominant deformation mechanism. Once the precipitates are sheared, the to-and-fro movement of dislocations during cyclic deformation generally leads to a softened region and causes strain localization. On the other hand, over-aged precipitates lead to cyclic hardening and homogeneous plastic deformation. In the current investigation, the average size of L₁₂ precipitates in AH+LTA condition was $\sim 2.2 \pm 1.3$ nm. Hence, the expected precipitate shearing mechanism during cyclic deformation explains the fatigue behavior of L₁₂ strengthened lamellar high entropy alloy. In a study on Inconel 825 alloy with L₁₂ precipitates, peak aged material exhibited lower crack growth rates as compared with the under-aged condition [30]. Overall, the presence of L₁₂ precipitates resulted in significant tensile strength increase, although no substantial variation in fatigue lives was noted. To further understand the difference between fatigue failure mechanism with and without L₁₂ precipitates, detailed post-fatigue deformation analysis including lateral surface analysis for PSB characterization and TEM analysis were carried out.

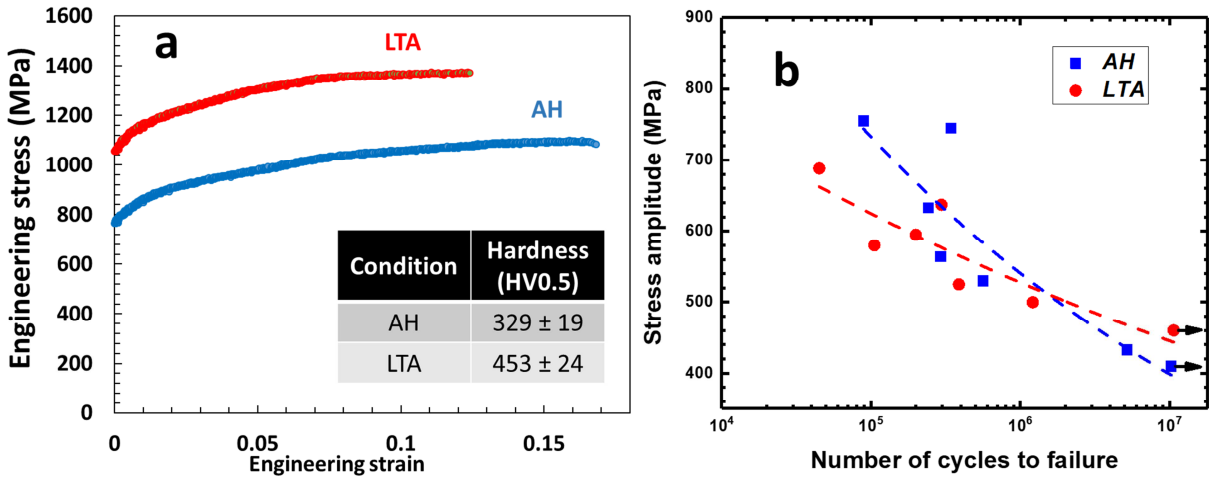


Figure 4. *Mechanical behavior of the alloy.* (a) Engineering stress-strain curve for both conditions, and (b) fatigue S-N data for both conditions.

3.3 Fatigue failure mechanism

3.3.1 Examination using scanning electron microscopy

Fatigue failure mechanism for both microstructural conditions is discussed here. Surface extrusion and intrusion revealed in EBSD PRIAS top map (pattern region of interest analysis system, (Figure 5 (a)) confirm PSBs near the major crack. In both conditions, high magnification SEM images revealed fine PSBs had formed (Figure 5). In addition to stress concentration that resulted in crack initiation along phase boundaries, fatigue cracks initiated and propagated along the PSBs (Figure 5 (a₁₋₃, b₁₋₃)). Consistent angles between and among various PSBs (Figure 5 (a₂₋₃, b₁₋₂) confirmed that various {111} <110> slip systems had been activated. Consequently, a zigzag crack propagation path was formed along PSBs. As mentioned above, in the case of a matrix with finely dispersed L1₂, nano-sized L1₂ precipitates were expected to be sheared by dislocations. With increasing fatigue cycles, the softened region turned into an easy path for dislocation movement, thereby creating PSBs. As a result, no significant difference between the two conditions was observed. Note that the lateral surface analysis was carried out after sample

failure. To thoroughly understand the fatigue cycles necessary to create PSBs in two conditions, interrupted cyclic testing should be conducted. Similar concepts have been proved in Ni-based superalloys, where by fine dispersed γ'' were sheared by dislocations during cyclic fatigue testing [31]–[32].

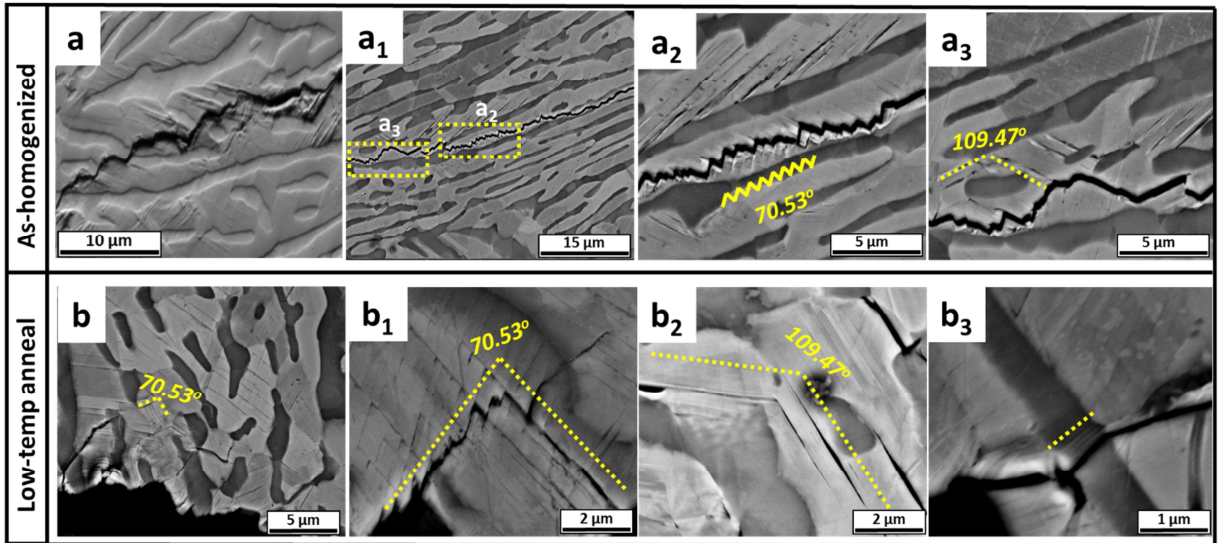


Figure 5. Post-deformation microstructures. (a) PRIAS map confirms the presence of PSBs and (a₁–₃) BSE images of the slip bands in as-homogenized condition. (b, b₁–₃) BSE images of the slip bands in low-temperature annealing condition.

3.3.2 Examination using transmission electron microscopy

Now a post-deformation analysis of the fatigued samples using TEM is presented. The samples were prepared using FIB lift-out technique and were taken from a region close to the major crack in both conditions. Figure 6 shows after-deformation TEM results from the AH condition, and focuses on deformation features within the FCC phase. Under stress amplitude used for fatigue testing, the hard intermetallic B2 phase undergoes minimum deformation. The BFTEM image in Figure 6 (a) captures a PSB formed in the FCC matrix. A two-beam condition with $g = \{200\}$ was used to capture defects after cyclic loading. Note that fine-scale B2 grains within the FCC lamelle are not sheared by the PSBs (yellow arrow in Figure 6 (a)). However, extensive

dislocation pile-up is observed around the B2 phase (Figure 6 (b)). Earlier, in Figures 3 (a) and (b), we presented the disordered FCC phase in AH condition. Nonetheless, the bowing or bending of dislocations, or dislocation interactions within the matrix (Figure 6 (a), marked by red arrows) appeared within the FCC phase. Lerch et al. [33] confirmed that such dislocation substructures are common within PSBs in Ni-based superalloys.

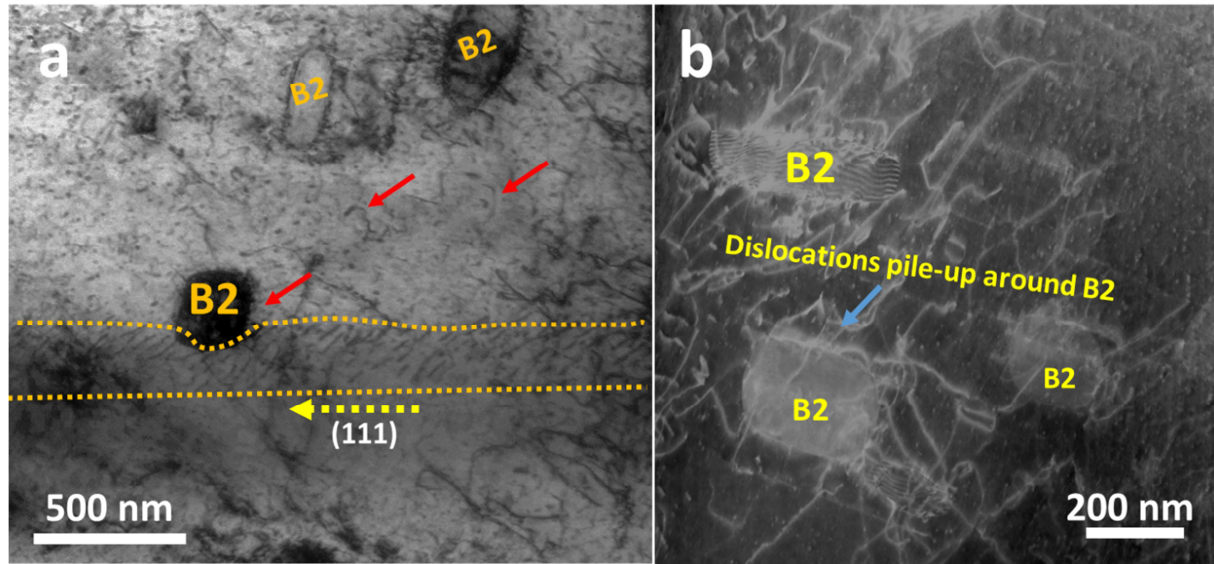


Figure 6. (a) BFTEM results for AH condition, and (b) higher magnification TEM shows dislocation pile-ups around fine-scaled B2 phase.

Figure 7 presents TEM results from the AH+LTA condition. Multiple PSBs are captured in the FCC phase, which is expected as per SEM results. Figure 7 (a) shows the FCC lamella containing PSBs highlighted by dashed arrows. The SADPs ((b1) and (b2)) were taken from outside and within the band, respectively. Note that the superlattice corresponding to the ordered L₁₂ phase diminished within the band. Such observation confirms shearing of the nano-scale L₁₂ phase during cyclic loading [34]. Similar to the AH condition, dislocation pile-ups were evident

around the fine B2 phase (Figure 7(c)). Another interesting takeaway is that no evidence of formation of deformation nano-twins was observed for both conditions.

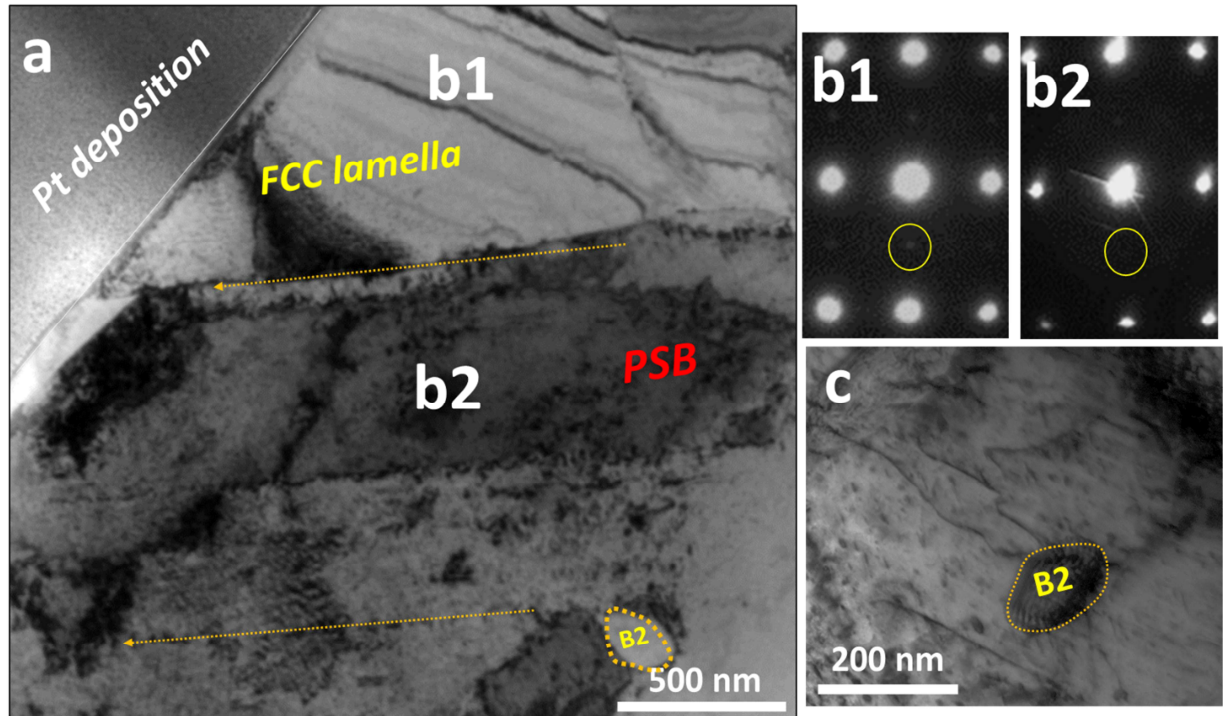


Figure 7. (a) BFTEM results for AH+LTA condition, (b₁) SADPs obtained from FCC lamella, (b₂) SADPs obtained from PSB, and (c) higher magnification TEM shows dislocation pile-ups around fine-scaled B2 phase.

3.4 Fractography

Fractography analysis was done to investigate fracture surface features and to correlate them to failure mechanisms mentioned above; Figure 8 shows the fracture surface of a sample tested at 550 MPa stress amplitude which failed at around 1.98×10^6 cycles. Three typical stages of fatigue failure observed on the fracture surface (Figure 8 (a)) included multiple Stage I crack initiation sites. Clear decohesion of phase boundaries with lamellar structure was seen in Figure 8 (a, a₁). Crack propagation with fine fatigue striations indicates the presence of Stage II (Figure 8 (a₃)), marked with yellow arrows. Persistent slip bands in the FCC matrix are highlighted in Figure 8

(a₂) (dashed yellow lines). Further, a typical overload fracture morphology (Stage III) displays typical cleavage failure (Figure 8 (a₄)). The cleavage feature agrees with the limited tensile ductility observed in the previous section. Typically, dimples appear in ductile materials, wherein brittle materials cleavage features present in the final rupture state [21].

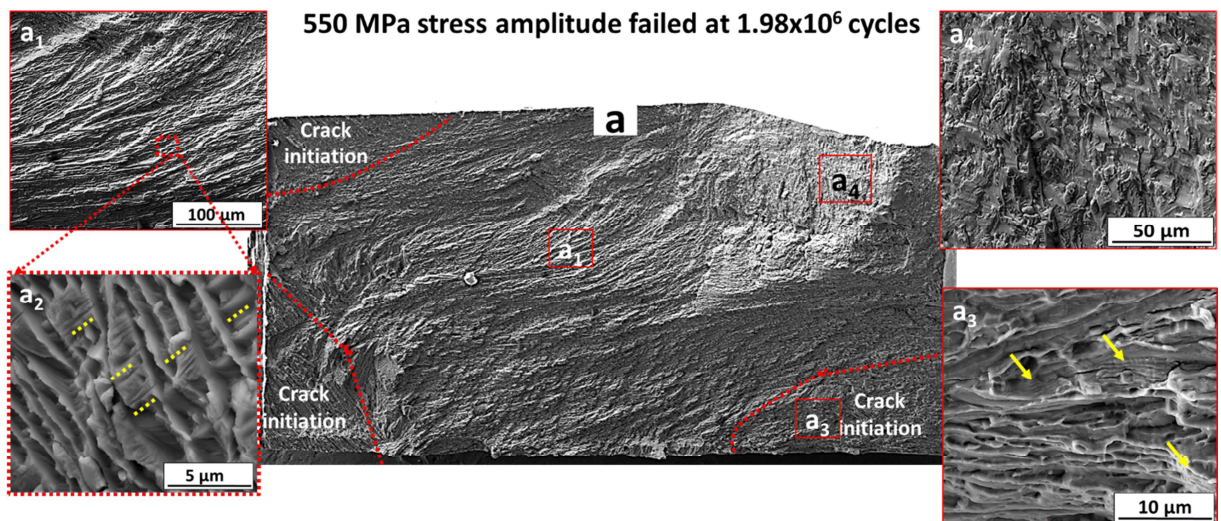


Figure 8. *Fractography analysis*. (a) Fracture surface of a sample tested at 550 MPa stress amplitude after 1.98×10^6 cycles, (a₁) fracture surface reveals decohesion at the phase boundaries, (a₂) cleavage fracture morphology, (a₃) fatigue striations, and (a₄) FCC slip bands on the fracture surface.

4. Conclusions

Fatigue behavior of the alloy of the Al_{0.7}CoCrFeNi with two heat treatment conditions was studied, and following conclusions can be drawn:

1. The improvement of tensile strength from AH condition to AH+LTA condition was attributed to the formation of nano-sized coherent L1₂ precipitates in the FCC matrix. However, strength-ductility trade-off was observed.

2. Fatigue cracks initiate and propagate along the B2/FCC lamellar phase boundary, as do PSBs in the FCC matrix. A zigzag crack-propagating pattern was due to the activation of various slip systems.
3. Coherent nano-sized L₁₂ precipitates did not improve fatigue property, as these precipitates are believed to have been sheared during cyclic loading.
4. TEM observations confirmed that PSBs are forming in the FCC lamelle, wherein low-temperature annealed condition nanosized L₁₂ phases are sheared. Therefore, no apparent changes in fatigue properties were observed.

Acknowledgment

Authors gratefully acknowledge the support of National Science Foundation through grant no 1435810. Authors also thank the Materials Research facility for the microscopy facility.

Data availability statement

The raw/processed data required to reproduce these findings cannot be shared at this time as the data also forms part of an ongoing study.

References

- [1] J. Yeh, S. Chen, S. Lin, J. Gan, T. Chin, T. Shun, C. Tsau, S. Chang, Nanostructured high-entropy alloys with multiple principal elements: novel alloy design concepts and outcomes, *Adv. Eng. Mater.* 6 (2004) 299-303. <https://doi.org/10.1002/adem.200300567>
- [2] B. Cantor, I. Chang, P. Knight, A. Vincent, Microstructural development in equiatomic multicomponent alloys, *Mater. Sci. Eng. A.* 375 (2004) 213-218. <https://doi.org/10.1016/j.msea.2003.10.257>
- [3] Y. Ye, Q. Wang, J. Lu, C. Liu, Y. Yang, High-entropy alloy: challenges and prospects, *Mater. Today.* 19 (2016) 349-362. <https://doi.org/10.1016/j.mattod.2015.11.026>

- [4] O. Senkov, G. Wilks, J. Scott, D. Miracle, Mechanical properties of $\text{Nb}_{25}\text{Mo}_{25}\text{Ta}_{25}\text{W}_{25}$ and $\text{V}_{20}\text{Nb}_{20}\text{Mo}_{20}\text{Ta}_{20}\text{W}_{20}$ refractory high entropy alloys, *Intermetallics*. 19 (2011) 698-706. <https://doi.org/10.1016/j.intermet.2011.01.004>
- [5] Y. Kao, T. Chen, S. Chen, J. Yeh, Microstructure and mechanical property of as-cast,-homogenized, and-deformed $\text{Al}_x\text{CoCrFeNi}$ ($0 \leq x \leq 2$) high-entropy alloys, *J Alloy Compd.* 488 (2009) 57-64. <https://doi.org/10.1016/j.jallcom.2009.08.090>
- [6] Z. Li, K.G. Pradeep, Y. Deng, D. Raabe, C.C. Tasan, Metastable high-entropy dual-phase alloys overcome the strength-ductility trade-off, *Nature*. 534 (2016) 227.
- [7] W. Wang, W. Wang, S. Wang, Y. Tsai, C. Lai, J. Yeh, Effects of Al addition on the microstructure and mechanical property of $\text{Al}_x\text{CoCrFeNi}$ high-entropy alloys, *Intermetallics*. 26 (2012) 44-51. <https://doi.org/10.1016/j.intermet.2012.03.005>
- [8] D. Miracle, O. Senkov, A critical review of high entropy alloys and related concepts, *Acta Mater.* 122 (2017) 448-511. <https://doi.org/10.1016/j.actamat.2016.08.081>
- [9] S. Nene, M. Frank, K. Liu, S. Sinha, R. Mishra, B. McWilliams, K. Cho, Reversed strength-ductility relationship in microstructurally flexible high entropy alloy, *Scr. Mater.* 154 (2018) 163-167. <https://doi.org/10.1016/j.scriptamat.2018.05.043>
- [10] S. Liu, Y. Wu, H. Wang, J. He, J. Liu, C. Chen, X. Liu, H. Wang, Z. Lu, Stacking fault energy of face-centered-cubic high entropy alloys, *Intermetallics*. 93 (2017) 269-273. <https://doi.org/10.1016/j.intermet.2017.10.004>
- [11] S. Gangireddy, B. Gwalani, V. Soni, R. Banerjee, R.S. Mishra, Contrasting mechanical behavior in precipitation hardenable $\text{Al}_x\text{CoCrFeNi}$ high entropy alloy microstructures: Single phase FCC vs. dual phase FCC-BCC, *Mater. Sci. Eng. A*. 739 (2019) 158-166. <https://doi.org/10.1016/j.msea.2018.10.021>
- [12] G. Liu, L. Liu, X. Liu, Z. Wang, Z. Han, G. Zhang, A. Kostka, Microstructure and mechanical properties of Al 0.7 CoCrFeNi high-entropy-alloy prepared by directional solidification, *Intermetallics*. 93 (2018) 93-100. <https://doi.org/10.1016/j.intermet.2017.11.019>
- [13] K. Liu, M. Komarasamy, B. Gwalani, S. Shukla, R.S. Mishra, Fatigue behavior of ultrafine grained triplex $\text{Al}_{0.3}\text{CoCrFeNi}$ high entropy alloy, *Scr. Mater.* 158 (2019) 116-120. <https://doi.org/10.1016/j.scriptamat.2018.08.048>
- [14] S. Shukla, T. Wang, S. Cotton, R.S. Mishra, Hierarchical microstructure for improved fatigue properties in a eutectic high entropy alloy, *Scr. Mater.* 156 (2018) 105-109. <https://doi.org/10.1016/j.scriptamat.2018.07.022>
- [15] M.A. Hemphill, T. Yuan, G. Wang, J. Yeh, C. Tsai, A. Chuang, P. Liaw, Fatigue behavior of Al 0.5 CoCrCuFeNi high entropy alloys, *Acta Mater.* 60 (2012) 5723-5734. <https://doi.org/10.1016/j.actamat.2012.06.046>

- [16] Z. Tang, T. Yuan, C. Tsai, J. Yeh, C.D. Lundin, P.K. Liaw, Fatigue behavior of a wrought Al 0.5 CoCrCuFeNi two-phase high-entropy alloy, *Acta Mater.* 99 (2015) 247-258. <https://doi.org/10.1016/j.actamat.2015.07.004>
- [17] T. Niendorf, T. Wegener, Z. Li, D. Raabe, Unexpected cyclic stress-strain response of dual-phase high-entropy alloys induced by partial reversibility of deformation, *Scr. Mater.* 143 (2018) 63-67. <https://doi.org/10.1016/j.scriptamat.2017.09.013>
- [18] K. Liu, S.S. Nene, M. Frank, S. Sinha, R.S. Mishra, Metastability-assisted fatigue behavior in a friction stir processed dual-phase high entropy alloy, *Mater Res Lett.* 6 (2018) 613-619. <https://doi.org/10.1080/21663831.2018.1523240>
- [19] K. Tanaka, T. Mura, A theory of fatigue crack initiation at inclusions, *Metall Mater Trans A.* 13 (1982) 117-123. <https://doi.org/10.1007/BF02642422>
- [20] R. Ritchie, Mechanisms of fatigue crack propagation in metals, ceramics and composites: role of crack tip shielding, *Mater. Sci. Eng. A.* 103 (1988) 15-28. [https://doi.org/10.1016/0025-5416\(88\)90547-2](https://doi.org/10.1016/0025-5416(88)90547-2)
- [21] S. Suresh, *Fatigue of Materials*, Second ed., Cambridge university press, Cambridge 1998.
- [22] K.K. Sankaran, R.S. Mishra, *Metallurgy and Design of Alloys with Hierarchical Microstructures*, First ed., Elsevier, Kidlington, 2017.
- [23] P. Lukáš, L. Kunz, Role of persistent slip bands in fatigue, *Philos. Mag.* 84 (2004) 317-330. <https://doi.org/10.1080/14786430310001610339>
- [24] M.D. Sangid, The physics of fatigue crack initiation, *Int. J. Fatigue.* 57 (2013) 58-72. <https://doi.org/10.1016/j.ijfatigue.2012.10.009>
- [25] P. Lukáš, L. Kunz, Role of persistent slip bands in fatigue, *Philos. Mag.* 84 (2004) 317-330 <https://doi.org/10.1080/14786430310001610339>.
- [26] P. Hansson, S. Melin, Simulation of simplified zigzag crack paths emerging during fatigue crack growth, *Eng. Fract. Mech.* 75 (2008) 1400-1411. <https://doi.org/10.1016/j.engfracmech.2007.07.002>
- [27] B. Gwalani, V. Soni, M. Lee, S. Mantri, Y. Ren, R. Banerjee, Optimizing the coupled effects of Hall-Petch and precipitation strengthening in a Al0. 3CoCrFeNi high entropy alloy, *Mater Des.* 121 (2017) 254-260. <https://doi.org/10.1016/j.matdes.2017.02.072>
- [28] P. De, C. Obermark, R. Mishra, Development of a reversible bending fatigue test bed to evaluate bulk properties using sub-size specimens, *J Test Eval.* 36 (2008) 402-405.
- [29] L. Garimella, P. Liaw, D. Klarstrom, Fatigue behavior in nickel-based superalloys: a literature review, *JOM.* 49 (1997) 67-71. <https://doi.org/10.1007/BF02914771>

[30] L. Bartosiewicz, A. Krause, A. Spis, J. Raghavan, S. Putatunda, Fatigue crack growth behavior of a solid solution-strengthened nickel-base superalloy (Incoloy 825), *J Mater Eng Perform.* 1 (1992) 67-74. <https://doi.org/10.1007/BF02650035>

[31] G.V. Smith, Ductility and toughness considerations in elevated temperature service, San Francisco, Calif, 1978.

[32] H. Ghonem, D. Zheng, Depth of intergranular oxygen diffusion during environment-dependent fatigue crack growth in alloy 718, *Mater. Sci. Eng. A.* 150 (1992) 151-160. [https://doi.org/10.1016/0921-5093\(92\)90107-C](https://doi.org/10.1016/0921-5093(92)90107-C)

[33] B.A. Lerch, N. Jayaraman, S.D. Antolovich, A study of fatigue damage mechanisms in Waspaloy from 25 to 800 C, *Mater. Sci. Eng.* 66 (1984) 151-166. [https://doi.org/10.1016/0025-5416\(84\)90177-0](https://doi.org/10.1016/0025-5416(84)90177-0)

[34] S.D. Antolovich, Microstructural aspects of fatigue in Ni-base superalloys, *Philos. Trans. Royal Soc. A.* 373 (2015) 20140128. <https://doi.org/10.1098/rsta.2014.0128>